Topics in Current Chemistry (2022) 380:15
https://doi.org/10.1007/s41061-022-00366-w

REVIEW

NAST: Nonadiabatic Statistical Theory Package for Predicting Kinetics of Spin-Dependent Processes

Vsevolod D. Dergachev[1] · Mitra Rooein[1] · Ilya D. Dergachev[1] · Aleksandr O. Lykhin[1,2] · Robert C. Mauban[1] · Sergey A. Varganov[1]

Received: 3 September 2021 / Accepted: 15 January 2022

Abstract

We present a nonadiabatic statistical theory (NAST) package for predicting kinetics of spin-dependent processes, such as intersystem crossings, spin-forbidden unimolecular reactions, and spin crossovers. The NAST package can calculate the probabilities and rates of transitions between the electronic states of different spin multiplicities. Both the microcanonical (energy-dependent) and canonical (temperature-dependent) rate constants can be obtained. Quantum effects, including tunneling, zero-point vibrational energy, and reaction path interference, can be accounted for. In the limit of an adiabatic unimolecular reaction proceeding on a single electronic state, NAST reduces to the traditional transition state theory. Because NAST requires molecular properties at only a few points on potential energy surfaces, it can be applied to large molecular systems, used with accurate high-level electronic structure methods, and employed to study slow nonadiabatic processes. The essential NAST input data include the nuclear Hessian at the reactant minimum, as well as the nuclear Hessians, energy gradients, and spin–orbit coupling at the minimum energy crossing point (MECP) between two states. The additional computational tools included in the NAST package can be used to extract the required input data from the output files of electronic structure packages, calculate the effective Hessian at the MECP, and fit the reaction coordinate for more advanced NAST calculations. We describe the theory, its implementation, and three examples of application to different molecular systems.

Keywords Intersystem crossings · Spin-forbidden reactions · Spin–orbit coupling · Reaction rates

This article is part of the Topical Collection "New Horizon in Computational Chemistry Software"; edited by Michael Filatov, Cheol H. Choi, and Massimo Olivucci.

✉ Sergey A. Varganov
svarganov@unr.edu

Extended author information available on the last page of the article

Published online: 24 February 2022

1 Introduction

Spin-dependent processes, including transitions between electronic states characterized by different values of total electron spin and magnetic quantum numbers, play an important role in many areas of atomic and molecular science. These include multi-state reactivity in transition-metal-based catalysis [1–6] and on semiconductor surfaces [7], design of photosensitizers for various applications [8–10], and development of single-molecule magnets for applications in quantum sensing, quantum computing, and spintronics [11–15]. For example, in photodynamic therapy, intersystem crossing (ISC) populates a manifold of low-lying triplet states of a photosensitizer. The following spin-allowed triplet–triplet reaction with molecular oxygen produces highly reactive oxygen species, which destroy cancer cells [8–10]. Delayed fluorescence in organic light-emitting diodes (OLEDs) is due to a thermally activated reverse ISC between close-lying excited triplet and singlet electronic states [16–20]. A nitrogen-vacancy (NV) center in diamond—one of the most promising candidates for a spin-based qubit—is initialized through the ISC between optically excited triplet and singlet states [13]. Photolysis of axial ligands from active sites of heme proteins proceeds via several ISCs on a femtosecond time scale [21–25]. Spin-forbidden low-energy reaction pathways have been proposed for the catalytic mechanisms of molecular hydrogen activation on the NiFe-hydrogenase metalloprotein [6] and the C–H bond activation on Fe (II) [3]. Many ligand–metal binding and dissociation reactions, such as the CO binding to $Fe(CO)_4$ [26, 27] and the diatomic molecules binding to the active site of heme proteins [28–30], are formally spin-forbidden. Spin crossovers and spin–spin magnetic exchange interactions in d^4–d^7 transition metal complexes play a fundamental role in the design of magnetic bistable materials [31–39].

Predicting kinetics of spin-dependent processes is important for understanding the mechanisms of thermally activated spin-forbidden reactions, ISCs in photochemistry, and spin crossovers in transition metal-based systems. There are two main approaches to calculate the rate constants and lifetimes of electronic states in spin-dependent processes. In ab initio nonadiabatic molecular dynamics, the classical or quantum nuclei are time propagated on the coupled potential energy surfaces (PESs) of multiple spin states [40–49], and the time evolution of nuclear trajectories is used to statistically describe the population transfer between the interacting electronic states. Such molecular dynamics simulations can be very accurate; however, they often require thousands of electronic structure calculations and can be computationally expensive if not prohibitive. An alternative nonadiabatic statistical theory (NAST) approach, also called nonadiabatic transition state theory [4, 26, 30, 50–59], largely eliminates the computational burden by exploring only the critical points on PESs. This allows NAST to be used with the high-level electronic structure methods and model even slow nonadiabatic processes intractable for molecular dynamics. NAST can be viewed as an extension of traditional transition state theory (TST) [60–65] to the nonadiabatic processes. Similarly to TST, NAST assumes that (1) intramolecular energy is statistically

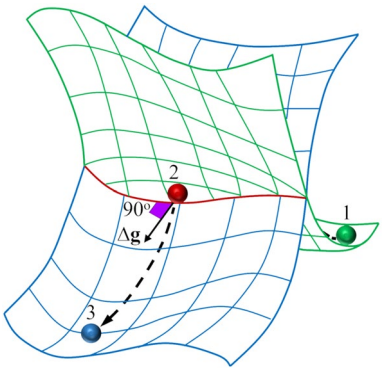

Fig. 1 Intersection of potential energy surfaces of two electronic states with different spin multiplicities. Point 1 is the reactant minimum, point 2 is the minimum energy crossing point (MECP), point 3 is the product minimum, and $\Delta\mathbf{g} = |\mathbf{g}_1 - \mathbf{g}_2|$ is the gradient vector orthogonal to the crossing seam and aligned with the reaction coordinate at the MECP. The dashed curve shows the minimum energy path connecting the MECP with the reactant and product minima

distributed among the molecular degrees of freedom (DOF) and (2) a one-dimensional reaction coordinate can be separated from the remaining spectator DOF. Both microcanonical (energy-dependent) and canonical (temperature-dependent) ensembles can be used to describe internal states leading to two formulations of NAST. Transitions between PESs of two electronic states with different spin multiplicities are driven by various spin-dependent interactions, among which the spin–orbit coupling (SOC) is often the strongest [66–69]. The crossing seam between such two PESs is $3N-7$ dimensional, where N is the number of atoms in a molecule, and the seven omitted dimensions include three translational, three rotational, and a reaction coordinate DOF. It is also assumed that nonadiabatic transitions between two crossing PESs can be described by effective transitions at a minimum energy crossing point (MECP) on the seam [4], which plays a similar role to that of a saddle point in TST (Fig. 1). At the MECP, the reaction coordinate is orthogonal to the rest of the (spectator) DOF. To evaluate the rate constant using NAST, the nuclear Hessian at the reactant minimum, as well as the energy gradients, nuclear Hessians, and the SOC at MECP, are needed. A more advanced treatment requires the knowledge of one-dimensional minimum energy paths from the MECP to the reactant and product minima [59, 70]. The statistical nature of NAST makes it relatively simple to account for the quantum effects, such as tunneling and zero-point vibrational energy (ZPE) [59].

In this article, we present the NAST package for investigating the mechanisms and predicting the rates of spin-dependent processes. The package includes an implementation of NAST and additional computational tools for processing the output of electronic structure calculations. In Sect. 2, we describe the fundamentals of NAST. In Sect. 3, we discuss the NAST package capabilities and implementation. In Sect. 4, we present several examples of NAST application. In conclusion, we summarize the main strengths and discuss future extensions of NAST.

2 Nonadiabatic Statistical Theory

2.1 Microcanonical Rate Constants

The microcanonical rate constant $k(E)$ of a unimolecular reaction is calculated as a function of the internal (rovibrational) energy E,

$$k(E) = \sigma \frac{N_{\mathrm{X}}(E)}{h\rho_{\mathrm{R}}(E)}, \tag{1}$$

$$N_{\mathrm{X}}(E) = \int_0^E \rho_{\mathrm{X}}\left(E - \varepsilon_{\perp}\right) P\left(\varepsilon_{\perp}\right) \mathrm{d}\varepsilon_{\perp}, \tag{2}$$

$$\sigma = \frac{\sigma_{\mathrm{R}}}{\sigma_{\mathrm{X}}} \gamma_{\mathrm{X}}, \tag{3}$$

where $N_{\mathrm{X}}(E)$ is the effective number of states at the MECP, ρ_{R} and ρ_{X} are the densities of rovibrational states at the reactant and MECP, respectively, and h is the Planck constant. Calculations of the densities of rovibrational states are described in the Supplementary Information (SI). The interstate transition probability $P\left(\varepsilon_{\perp}\right)$ is a function of the energy $\varepsilon_{\perp}$ partitioned in the reaction coordinate orthogonal to the crossing seam. The reaction path degeneracy σ is defined in terms of the symmetry numbers of reactant (σ_R) and MECP (σ_{X}) [71], and the number of chiral MECP isomers (γ_{X}) [72].

2.2 Microcanonical Transition Probabilities

The most popular ways to calculate the interstate transition probability $P\left(\varepsilon_{\perp}\right)$ in Eq. (2) are the double-passage Landau–Zener (LZ) and weak coupling (WC) formulas [4, 55, 73, 74]. These formulas yield a cumulative probability of transition at the MECP for the forward (primary passage) and backward (secondary passages) motions along the reaction coordinate,

$$P_{\mathrm{LZ}}\left(\varepsilon_{\perp}\right) = p_{\mathrm{LZ}} + \left(1 - p_{\mathrm{LZ}}\right) p_{\mathrm{LZ}} = 2p_{\mathrm{LZ}} - p_{\mathrm{LZ}}^2, \tag{4}$$

$$p_{\mathrm{LZ}}\left(\varepsilon_{\perp}\right) = 1 - \exp\left(-\frac{2\pi H_{\mathrm{SO}}^2}{\hbar |\Delta \mathbf{g}|} \sqrt{\frac{\mu_{\perp}}{2\left(\varepsilon_{\perp} - E_X\right)}} \right), \tag{5}$$

$$P_{\mathrm{WC}}\left(\varepsilon_{\perp}\right) = 4\pi^2 H_{\mathrm{SO}}^2 \left(\frac{2\mu_{\perp}}{\hbar^2 \overline{\mathbf{g}} |\Delta \mathbf{g}|} \right)^{\frac{2}{3}} \mathrm{Ai}^2 \left[-\left(\varepsilon_{\perp} - E_X\right) \left(\frac{2\mu_{\perp} |\Delta \mathbf{g}|^2}{\hbar^2 \overline{\mathbf{g}}^4} \right)^{\frac{1}{3}} \right], \tag{6}$$

where p_{LZ} is the single-passage LZ probability, H_{SO} is the spin–orbit coupling constant, and $\hbar$ is the reduced Planck constant. The norm of the gradient parallel to the reaction coordinate $|\Delta\mathbf{g}| = |\mathbf{g}_1 - \mathbf{g}_2|$ and the mean gradient $\bar{\mathbf{g}} = \left(|\mathbf{g}_1||\mathbf{g}_2|\right)^{1/2}$ are defined in terms of the gradients of two crossing PESs at the MECP, $\mathbf{g}_1$ and $\mathbf{g}_2$. In Eqs. (5 and 6), $\mu_\perp$ is the reduced mass for the motion along the reaction coordinate, and E_X is the MECP energy barrier with respect to the reactant minimum. In Eq. (6), Ai is the Airy function.

To account for ZPE, the MECP energy can be redefined as $E_X \rightarrow E_X + ZPE_X - ZPE_R$. For a nonlinear molecule, the zero-point energies at the reactant minimum and MECP are defined as:

$$ZPE_R = \frac{1}{2}\sum_{i=1}^{3N-6} \hbar\omega_i^R, \tag{7}$$

$$ZPE_X = \frac{1}{2}\sum_{i=1}^{3N-7} \hbar\omega_i^X, \tag{8}$$

where ω_i^R and ω_i^X are the fundamental transition frequencies of the reactant and MECP, respectively. In Eq. (7), index i runs over $3N-6$ vibrational DOF, while only $3N-7$ DOF orthogonal to the reaction coordinate contribute to ZPE at the MECP. Note that using ZPE_X at the classical turning point along the minimum energy reaction path is equivalent to the zero-curvature tunneling approximation in TST, where the density of the rovibrational states is approximated by the density at TS, and the effective TS barrier is reduced by the difference between ZPE_R and ZPE_{TS}.

The LZ probability is defined only at the reaction energy $\varepsilon_\perp$ above the MECP, and therefore does not account for quantum tunneling through the MECP barrier. In addition, the LZ probability formula does not describe the quantum interference between primary and secondary passages at the MECP [4]. These two quantum effects are included in the WC probability formula. However, both the LZ and WC formulas are only valid within the limited region of the parameters $\varepsilon_\perp$, $\mu_\perp$, H_{SO} and the energy gradients. For example, the WC formula can predict a greater than unit probability of transition if the interacting states are strongly coupled, as is often the case in the complexes containing second- and third-row transition metals [4]. In addition, the LZ and WC formulas assume a linear behavior of the two crossing potentials, which is often a reasonable approximation in the vicinity of the MECP but not in the regions closer to the reactant and product minima. A more sophisticated approach to predict transition probabilities, which does not suffer from these limitations, has been introduced by Zhu and Nakamura (ZN) [70, 75–79]. The ZN probability expressions require the knowledge of the entire one-dimensional minimum energy path connecting the MECP to the reactant and product minima. This path can be obtained in either spin-diabatic or spin-adiabatic representations [49]. The ZN theory distinguishes two intersection types between PESs: a sloped intersection $\left(\mathbf{g}_1 \cdot \mathbf{g}_2 > 0\right)$ and a peaked intersection $\left(\mathbf{g}_1 \cdot \mathbf{g}_2 < 0\right)$ (Fig. S1). Currently, in the NAST package, the ZN probability is implemented only for a sloped intersection in the spin-adiabatic representation. Because most of the electronic structure

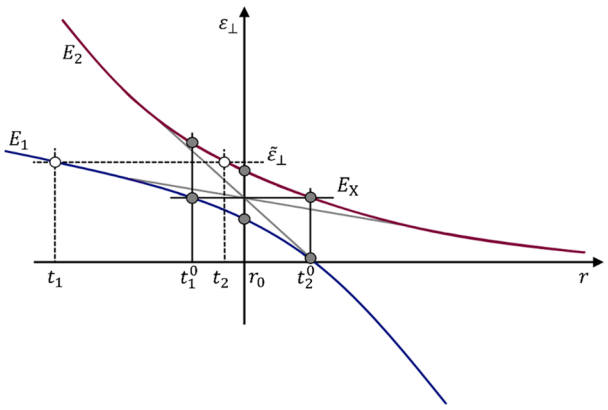

Fig. 2 Sloped intersection of two spin-adiabatic potentials with the energies E_1 (blue) and E_2 (red) along the reaction coordinate r. Points r_0, t_1^0, t_2^0, t_1, and t_2 are defined in the text

calculations produce spin-diabatic PESs, the adiabatic potentials are obtained by diagonalizing the following matrix:

$$\begin{pmatrix} E_1^d(r) & H_{SO} \\ H_{SO} & E_2^d(r) \end{pmatrix}, \tag{9}$$

where E_1^d and E_2^d are the spin-diabatic energies of two electronic states with arbitrary spin multiplicities, r is the arc length along the minimum energy reaction path in mass-scaled coordinates [80] with the reduced mass set to 1 amu, and H_{SO} is the spin–orbit coupling constant at the MECP. The diagonalization of the matrix defined by Eq. (9) produces two eigenvalues corresponding to the adiabatic (spin-mixed) state energies, E_1 and E_2 (Fig. 2). The ZN double-passage transition probability is given by

$$P_{ZN}(\varepsilon_\perp) = 4p_{ZN}(1 - p_{ZN})\sin^2(\psi), \tag{10}$$

where ψ is the overall transition phase. The single passage probability p_{ZN} defined in the SI depends on several parameters that are functions of the energies at the smallest energy gap point r_0, the turning points at the MECP energy t_1^0 and t_2^0, and the turning points t_1 and t_2 corresponding to the specific value of the energy $\varepsilon_\perp$ (Fig. 2).

2.3 Canonical Rate Constants

A canonical, temperature-dependent rate constant can be obtained by averaging the microcanonical rate constant (Eq. 1) over the internal energy Boltzmann distribution, leading to the following expression:

$$k(T) = \frac{\sigma}{hQ_{\mathrm{R}}(T)} \int_0^\infty N_{\mathrm{X}}(E) e^{-E/k_{\mathrm{B}}T} \mathrm{d}E, \tag{11}$$

$$Q_{\mathrm{R}}(T) = \int_0^\infty \rho_{\mathrm{R}}(E) e^{-E/k_{\mathrm{B}}T} \mathrm{d}E, \tag{12}$$

where Q_{R} is the partition function of the reactant, T is the temperature, and k_{B} is the Boltzmann constant.

2.4 Velocity-Averaged Probabilities

Velocity-averaged probabilities provide a simple estimate for the likelihood of spin-forbidden reaction mechanism as a function of temperature. The velocity-averaged single passage LZ probabilities (Eqs. 13 and 14) are derived by averaging the microcanonical LZ probability (Eq. 5) using the Maxwell–Boltzmann (MB) and normalized Kuki (K) distributions of the mass-weighted velocity $v^2 = 2\left(\varepsilon_\perp - E_{\mathrm{X}}\right)$ [6, 81]. The corresponding double-passage LZ probabilities can be obtained using Eq. (4). The velocity-averaged WC probabilities (Eqs. 15 and 16) can also be derived using the Maxwell–Boltzmann and normalized Kuki distributions. It is important to note that, in contrast to the microcanonical WC probability, the velocity-averaged WC probabilities do not account for quantum tunneling.

$$\langle p_{\mathrm{LZ}}(T)\rangle_{\mathrm{MB}} = 1 - \left(\frac{2}{\pi k_{\mathrm{B}}T}\right)^{\frac{1}{2}} \int_0^\infty \exp\left(-\frac{2\pi H_{\mathrm{SO}}^2 \mu_\perp^{1/2}}{\hbar|\Delta \mathbf{g}| v}\right) \exp\left(-\frac{v^2}{2k_{\mathrm{B}}T}\right) \mathrm{d}v, \tag{13}$$

$$\langle p_{\mathrm{LZ}}(T)\rangle_{\mathrm{K}} = 1 - \frac{1}{k_{\mathrm{B}}T} \int_0^\infty v \exp\left(-\frac{2\pi H_{\mathrm{SO}}^2 \mu_\perp^{1/2}}{\hbar|\Delta \mathbf{g}| v}\right) \exp\left(-\frac{v^2}{2k_{\mathrm{B}}T}\right) \mathrm{d}v, \tag{14}$$

$$\langle P_{\mathrm{WC}}(T)\rangle_{\mathrm{MB}} = \alpha \left(\frac{2}{\pi k_{\mathrm{B}}T}\right)^{\frac{1}{2}} \int_0^\infty \mathrm{Ai}^2\left(-\frac{1}{2} v^2 \mu_\perp \gamma\right) \exp\left(-\frac{v^2}{2k_{\mathrm{B}}T}\right) \mathrm{d}v, \tag{15}$$

$$\langle P_{\mathrm{WC}}(T)\rangle_{\mathrm{K}} = \frac{\alpha}{k_{\mathrm{B}}T} \int_0^\infty v \mathrm{Ai}^2\left(-\frac{1}{2} v^2 \mu_\perp \gamma\right) \exp\left(-\frac{v^2}{2k_{\mathrm{B}}T}\right) \mathrm{d}v, \tag{16}$$

$$\alpha = 4\pi^2 H_{\mathrm{SO}}^2 \left(\frac{2\mu_\perp}{\hbar^2 \overline{\mathbf{g}} |\Delta \mathbf{g}|}\right)^{\frac{2}{3}}, \tag{17}$$

$$\gamma = \left(\frac{2\mu_{\perp} |\Delta \mathbf{g}|^2}{\hbar^2 \overline{\mathbf{g}}^4} \right)^{\frac{1}{3}}. \tag{18}$$

2.5 Rate Constants and Transition Probabilities Between Individual M_S Components of Spin States

A simple approach to model transitions between electronic states with the different spin quantum numbers S and S' is to calculate the effective probabilities and rate constants accounting for all M_S components of the spin multiplets. In this approach, the effective SOC, also called the SOC constant, is obtained as the RMS of the couplings between individual M_S components,

$$H_{SO} = \left(\sum_{M_s=-S}^{S} \sum_{M_{S'}=-S'}^{S'} \left| \left\langle S, M_S \middle| \hat{H}_{SO} \middle| S', M_{S'} \right\rangle \right|^2 \right)^{1/2}. \tag{19}$$

In Eq. (19), $\hat{H}_{SO}$ is the spin–orbit operator; for example, from the Breit–Pauli Hamiltonian [67]. This approach is easy to justify for a singlet–triplet crossing with the MECP energy gap between the two spin-adiabatic states equal to $2H_{SO}$ [4]. However, for the states with higher spin multiplicities, for example a triplet–quintet crossing, there are multiple energy gaps between the adiabatic states. Therefore, employing a single effective SOC to calculate the transition probability and rate constant is not well justified.

This issue can be addressed by calculating the rate constants and transition probabilities between individual M_S components of the spin multiplets. As an example, for a singlet–triplet crossing, the non-zero spin–orbit coupling matrix elements are

$$z = \left\langle 0,0|\hat{H}_{SO}|1,-1 \right\rangle, \quad ib = \left\langle 0,0|\hat{H}_{SO}|1,0 \right\rangle, \quad z^* = \left\langle 0,0|\hat{H}_{SO}|1,+1 \right\rangle, \tag{20}$$

where z and z^* are complex conjugate to each other, and b is real. The single-passage LZ probabilities $p_{LZ}^{M_S,M_{S'}}(\varepsilon_{\perp})$ between the components M_S and $M_{S'}$ of the spin states $S = 0$ and $S' = 1$ read

$$p_{LZ}^{0,-1}(\varepsilon_{\perp}) = p_{LZ}^{0,+1}(\varepsilon_{\perp}) = 1 - \exp\left(-\frac{2\pi z z^*}{\hbar |\Delta \mathbf{g}|} \sqrt{\frac{\mu_{\perp}}{2(\varepsilon_{\perp} - E_X)}} \right), \tag{21}$$

$$p_{LZ}^{0,0}(\varepsilon_{\perp}) = 1 - \exp\left(-\frac{2\pi b^2}{\hbar |\Delta \mathbf{g}|} \sqrt{\frac{\mu_{\perp}}{2(\varepsilon_{\perp} - E_X)}} \right). \tag{22}$$

The double-passage probabilities $P_{LZ}^{0,\pm 1}$ and $P_{LZ}^{0,0}$ can be obtained from the single-passage probabilities (Eq. 4) and employed to calculate the microcanonical rate constants between individual M_S components,

$$k_{0,\pm1}(E) = \frac{\sigma}{h\rho_{\mathrm{R}}(E)} \int_0^E \rho_{\mathrm{X}}\left(E - \varepsilon_\perp\right) P_{\mathrm{LZ}}^{0,\pm1}\left(\varepsilon_\perp\right) \mathrm{d}\varepsilon_\perp, \tag{23}$$

$$k_{0,0}(E) = \frac{\sigma}{h\rho_{\mathrm{R}}(E)} \int_0^E \rho_{\mathrm{X}}\left(E - \varepsilon_\perp\right) P_{\mathrm{LZ}}^{0,0}\left(\varepsilon_\perp\right) \mathrm{d}\varepsilon_\perp. \tag{24}$$

The probabilities and rate constants between individual M_{S} components can be calculated for any pair of spin states with $|S - S'| = 1$, as shown in the SI for a triplet-quintet crossing.

2.6 Transition State Theory Rate Constants

For adiabatic reactions, both microcanonical and canonical NAST rate constants can be reduced to the traditional TST rate constants by replacing MECP with a transition state (TS) and the transition probability in Eq. (2) with the Heaviside step function [82]. The canonical TST rate constant, obtained by averaging the microcanonical constant over the Boltzmann internal energy distribution, is equivalent to the traditional analytical TST expression [4]:

$$k(T) = \sigma \frac{k_{\mathrm{B}}T}{h} \frac{Q_{\mathrm{TS}}}{Q_{\mathrm{R}}} e^{-E_{\mathrm{TS}}/k_{\mathrm{B}}T}, \tag{25}$$

where Q_{TS} and Q_{R} are partition functions of TS and reactant.

2.7 Effective Hessian

Calculation of the effective number of states $N_{\mathrm{X}}(E)$ defined in Eq. 2 requires the density of vibrational states at the MECP, which can be obtained using the harmonic vibrational analysis [83, 84]. Since MECP is not a stationary point on either of the two crossing PESs, a conventional vibrational analysis is not valid. The vibrational frequencies at the MECP can be obtained from the effective Hessian matrix calculated using the state-specific Hessians $\mathbf{H}_1$ and $\mathbf{H}_2$, and gradients at MECP [85]:

$$\mathbf{H}_{\mathrm{eff}} = \frac{|\mathbf{g}_1|\mathbf{H}_2 \pm |\mathbf{g}_2|\mathbf{H}_1}{|\mathbf{g}_1| \pm |\mathbf{g}_2|}. \tag{26}$$

The details of calculating the effective Hessian are given in the SI.

3 NAST Package Capabilities and Implementation

3.1 Forward and Reverse Rate Constants

By default, the NAST package calculates only forward rate constants with both the LZ and WC transition probabilities. A forward direction is defined as the transition from the higher energy spin state (reactant) to the lower energy spin state (product). Such calculations require molecular properties only at the reactant minimum and MECP. However, calculation of the reverse rate constants can be requested in the same run, if molecular properties at the product minimum are provided. For such reverse rate calculations, the above definition of reactant and product prevents the reverse unphysical tunneling to the region below the reactant minimum where the density of states is zero (Fig. 3). If only a forward rate constant with tunneling contribution is calculated, it is important to ensure that the reactant has a higher energy than the product to prevent contribution from unphysical tunneling to the rate constants. This is not required if the rate constants are calculated with the LZ probability or traditional TST, which do not account for tunneling. In the present implementation, the ZN transition probability can only be used to calculate a forward rate constant. For canonical rate constant calculations, the temperature range (default 290–300 K) and step (default 1 K) can be specified in the input file.

3.2 Transition Probabilities

The LZ, WC, and ZN probabilities (Eqs. 4–6 and 10) are used to calculate the microcanonical and canonical rate constants. The velocity-averaged LZ and WC probabilities (Eq. 13–16), which are calculated by default, can be used to obtain a qualitative understanding of the spin-dependent reaction kinetics. While calculations of the LZ and WC probabilities require molecular properties at reactants and MECP only, the ZN probability calculations require additional input data discussed together with the intrinsic reaction coordinate (IRC) fit code (Sect. 3.7).

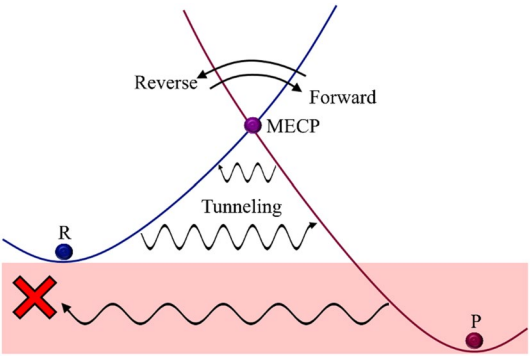

Fig. 3 Definition of forward and reverse directions. The region of reverse unphysical tunneling is shown by the red box

3.3 Rate Constants and Transition Probabilities Between Individual M_S Components of Spin States

In addition to effective transition probabilities and rate constants between the spin manifolds with the different values of quantum number S, the NAST package can calculate the transition probabilities and rate constants between individual M_S components of different spin manifolds. In the current implementation, the M_S-specific kinetics can be modeled only using the LZ formula. Such calculations can provide insight into the role of individual M_S components in the overall spin-dependent kinetics. Moreover, working in the basis of individual M_S components is necessary to study the effect of an external magnetic field on spin-dependent processes.

3.4 Rate Constants in Solution

Transition state theories for reactions in solution have been discussed extensively in previous works [60, 86–91]. In the current NAST implementation, the solution phase effects can be modeled by simply assuming that all molecular rotations are frozen. In such calculations, only vibrational states contribute to the total density of states, and contributions from rotational states are ignored.

3.5 Transition State Theory Rate Constants

The NAST package can calculate the traditional TST rate constants for single-state adiabatic reactions by replacing the MECP molecular properties with the TS properties (energy, vibrational frequencies, moments of inertia). Such TST calculations do not require spin–orbit couplings, energy gradients, or reduced mass, and can be invoked with a separate keyword.

3.6 Effective Hessian Tool *effhess*

The effective Hessian tool *effhess*, distributed as a part of the NAST package, calculates and diagonalizes the effective Hessian (Eq. 26) to generate the vibrational frequencies at the MECP, the reduced mass $\mu_\perp$, $|\Delta\mathbf{g}|$, and $\overline{\mathbf{g}}$. These quantities are needed for the following rate constant calculations. Currently, the tool can read the MECP energy gradient vectors and Hessian matrices from the output files generated by the GAMESS [92] and Molpro [93] electronic structure packages. The *effhess* tool generates a template of an input file for the main NAST code.

3.7 IRC Fitting Tool *ircfit*

The fitting tool *ircfit* produces the IRC potentials of two crossing spin states. These potentials are required for calculating the ZN probabilities. Currently, *ircfit*

can read only the GAMESS IRC output files. Here we summarize the *ircfit* algorithm; the details are included in the SI.

1. Perform two IRC calculations from MECP to the minima of reactant and product, generating the two sets of geometries $\{\boldsymbol{Q}_i, E_i\}_{X\to R}$ and $\{\boldsymbol{Q}_i, E_i\}_{X\to P}$, where $\boldsymbol{Q}_i$ and E_i are the coordinates and energy of molecular geometry i. Index i runs from 1 (MECP) to n for the reactant side of IRC and m for the product side.
2. Define $n+m$ points along the reaction coordinate as

$$r_j = \left(\sum_{p=1}^{3N} \left(dQ_{j,p} \right)^2 \right)^{1/2}, \tag{27}$$

   where $dQ_{j,p}$ is the difference between the coordinates of the reactant and the geometry $j \in [1, n+m]$.
3. Build the crossing potentials by fitting the two sets of points $\{r_i, E_i\}_{X\to R}$ and $\{r_i, E_i\}_{X\to P}$ with the fourth-order polynomials:

$$f(\mathbf{c}, r) = \sum_{q=0}^{4} c_q r^q. \tag{28}$$

The vector of coefficients $\mathbf{c}$ is obtained by minimizing the linear least-squares function

$$F = \sum_{i=1}^{k} \left(E_i - f\left(\mathbf{c}, r_i\right) \right)^2, \tag{29}$$

where $k=n$ for the reactant side of the fit, and $k=m$ for the product side. The coefficients of the polynomials, which represent spin-diabatic states, are used by the main NAST code to generate spin-adiabatic states (Eq. 9) required for the ZN probability calculations.

3.8 Modular Structure of the NAST Package

The NAST package consists of a collection of modules written in modern Fortran and runs under Linux (Fig. 4). The package manual contains a full list of the input file keywords that control the type of rate calculations. Most of the keywords have default values appropriate for the common calculation types. The effective Hessian tool *effhess* can be used to generate an input file template containing MECP

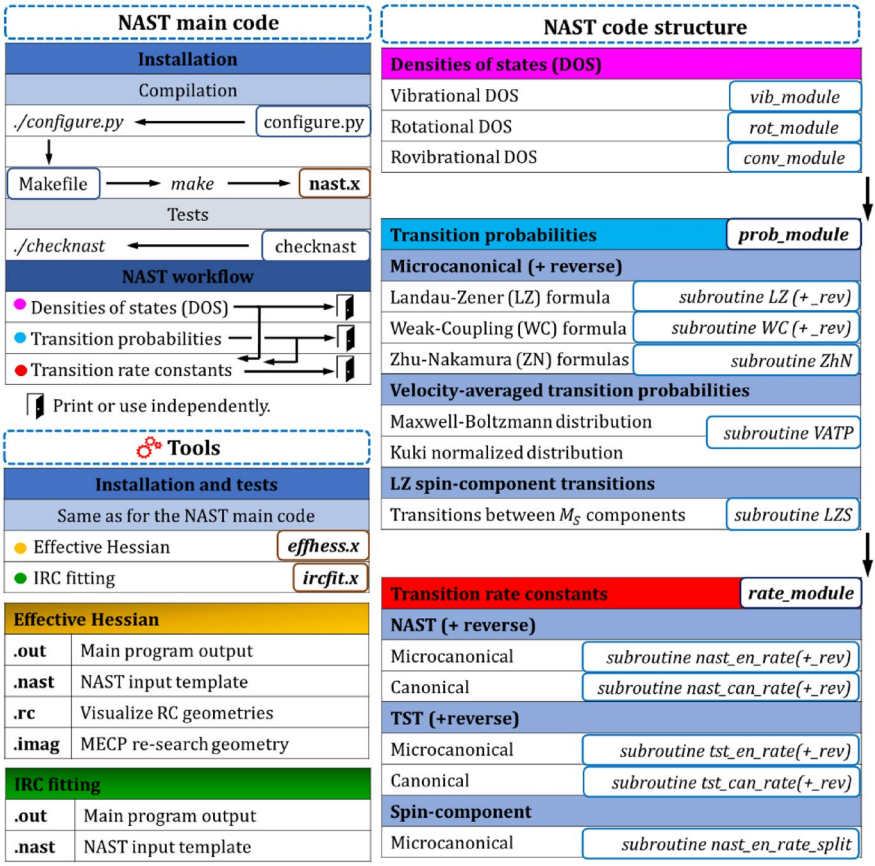

Fig. 4 Modular structure of the NAST package. The top left panel illustrates the main NAST code installation, testing, and workflow. The bottom left panel lists the output files of the effective Hessian (*effhess*) and IRC fitting (*ircfit*) tools. The right panel shows the main modules and subroutines of the NAST package

properties, further reducing the efforts required to set up a NAST calculation. The rest of the input data, including vibrational frequencies, moments of inertia, electronic energies, and SOC, must be extracted from the output of electronic structure calculations. The calculated canonical rate constants and velocity-averaged transition probabilities are saved to the main output file *nast.out*. Additional information, including microcanonical rate constants, transition probabilities, and density of states, are written to separate output files. The amount of output information can be controlled by the user.

Table 1 Canonical TST rate constants for isomerization of propylene oxide to acetone and propanal at T = 1000 K

Product	Source	E_{TS}, kcal·mol^{-1}	k_{1000}, s^{-1}
Acetone	NAST	53.2	67.8
	Analytical, Eq. (30)[a]	54.2	50.2
	Analytical, Eq. (25)	53.2	101.0
	Experiment[b]	–	30.0
Propanal	NAST	54.2	43.0
	Analytical, Eq. (30)[a]	54.4	69.6
	Analytical, Eq. (25)	54.2	88.6
	Experiment[b]	-	90.0

[a]Ref. [94]

[b]Experimental values are estimated from the log(k) vs. T plots of Ref. [95]

The NAST package requires an external math library. It has been tested with the Intel Math Kernel Library (MKL) but can be linked with other math libraries. The package has been successfully compiled and tested with the *gfortran* and *ifort* compilers. To streamline the package installation, the provided Python configuration script *configure.py* can be used to generate a *Makefile*. The Linux utility *make* is used to compile and link the executable *nast.x*. A new build can be tested by running the script *checknast* that executes several test examples. The installation and testing procedures are the same for the effective Hessian and IRC tools. The configuration and installation details are provided in the package manual.

4 Examples of Applications

4.1 Isomerization of Propylene Oxide to Acetone and Propanal

This example demonstrates how the NAST package can be used to calculate the reaction rates for single-state adiabatic reactions using the traditional TST. We consider the isomerization of propylene oxide to acetone and propanal, following the original theoretical work of Dubnikova and Lifshitz [94]. For each isomerization reaction, four canonical TST rate constants are compared: (1) predicted by the NAST package, (2) calculated analytically using Eq. (25), (3) calculated analytically using Eq. (30) below [94], and (4) obtained from an experiment [95]. In Ref. [94], the following equation is used:

$$k(T) = \sigma \frac{k_B T}{h} e^{-\Delta S^{\#}/R} e^{-\Delta H^{\#}/RT}, \tag{30}$$

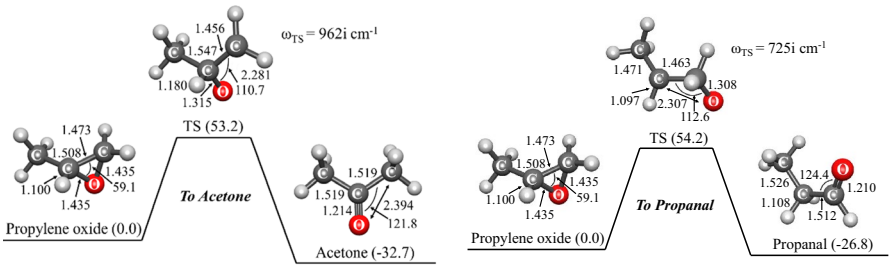

Fig. 5 Energies and structural parameters for the isomerization reactions of propylene oxide to acetone (left) and propanal (right). The relative CCSD(T) energies (kcal·mol^{-1}) listed in parenthesis are corrected with $\Delta ZPE = ZPE_X - ZPE_R$ calculated with B3LYP. Bond lengths and angles are in Å and degrees, respectively

where R is the universal gas constant; $\Delta S^{\#}$ and $\Delta H^{\#}$ are the entropy and enthalpy of activation, respectively. Because for a unimolecular reaction, $\Delta H^{\#} = E_{TS} + \Delta ZPE$, the activation enthalpy is equal to the ZPE-corrected electronic barrier between transition state and reactant. The input data for NAST were obtained from the B3LYP geometry optimization and Hessian calculations in GAMESS, and the single-point CCSD(T) energy calculations in Molpro. The cc-pVDZ basis set was used in all calculations. The partition functions Q_{TS} and Q_R used in Eq. (25) were taken from the GAMESS Hessian calculations. In Eq. (30), the original data from Table 1 of Dubnikova and Lifshitz [94] were used. The energy profiles for two isomerization reactions are shown in Fig. 5.

The NAST input file and parts of the output file are shown below.

```
&keys zpe = 1 tst = .true. &end          ! TST calculation with ZPE correction

&inputdata
freX = 263, 294, 374, 580, 729, 871, 886, 958, 999, 1081, 1118, 1241, 1283, 1357, 1434, 1452, 1471, 2296, 3026,
3092, 3118, ,3142, 3238      ! Vibrational frequencies (cm-1) of TS/MECP
freR = 240, 370, 416, 773, 848, 903, 974, 102, 1117, 1136, 1153, 1173, 1277, 1381, 1423, 1451, 1471, 1515, 3025,
3059, 3076, 3098, 3117, 3153 ! Vibrational frequencies (cm-1) of reactant
inertX = 170.850, 217.264, 351.144        ! Moments of inertia for TS/MECP
inertR = 100.305, 272.514, 305.514        ! Moments of inertia for reactant
enX = 0.09129754                          ! Energy of TS in hartree (program will add ΔZPE)
enR = 0.0                                 ! Energy of reactant in hartree
maxn = 30000                              ! Maximum energy bin - integration limit in cm-1
T1 = 1000                                 ! Initial temperature in K for canonical rate constant
&end
```

```
   ***********************************************************
   ~~~~~~~ NAST: Nonadiabatic Statistical Theory ~~~~~~~~
                ~~~~~ v. 2021.1 ~~~~~
   ***********************************************************
-----------------------------------------------------------
NAST control parameters and related data

zpe = 1    sp = F    zn = F    solution = F
tst = T    printmore = F    rev = F    extern = F
-----------------------------------------------------------
zpe = 1: ZPE correction scheme I (eliminates turning points below ZPE).
Electronic barrier from reactant to MECP is   20037 cm-1
ZPE of reactants =   18586 cm-1
ZPE of MECP =   17150 cm-1
ZPE-corrected MECP energy bin =  18602 cm

 ------------------------------------------------------------
          Start NAST calculation
 ------------------------------------------------------------

  1. Calculating densities of states

.....vibrational.
.....rotational.
.....rovibrational.

  2. Calculating microcanonical TST rate constant.
..... Done.

(The forward rate constant k(E) is multiplied by reaction path degeneracy equal to 1 )

          Canonical rate constant, k(T)

   T(K)    TST rate constant

 1000.0         6.78E+01

Total CPU time =    10.35
```

Table 1 shows the calculated and experimental rate constants for the isomerization of propylene oxide to acetone and propanal. The factor of two difference between the acetone rate constants calculated with two analytical expressions can be

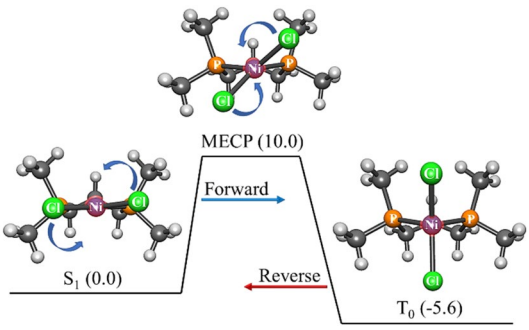

Fig. 6 Reaction path for the singlet–triplet isomerization of the Ni(dpp)Cl_2 model from the square-planar to tetrahedral geometry. The twist angle between the Cl–Ni–Cl and P–Ni–P planes is 6°, 42°, and 90° for the singlet, MECP, and triplet geometries, respectively. The phenyl groups of Ni(dpp)Cl_2 are replaced with the methyl groups

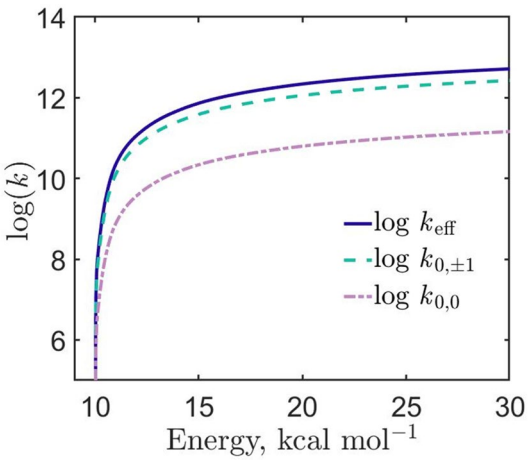

Fig. 7 The microcanonical rate constants $k_{0,0}$ and $k_{0,+1} = k_{0,-1}$ for transitions between the M_S components of the singlet and triplet states calculated using the LZ probabilities. The effective rate constant k_{eff} corresponds to the overall transition between the singlet state and all three components of the triplet state

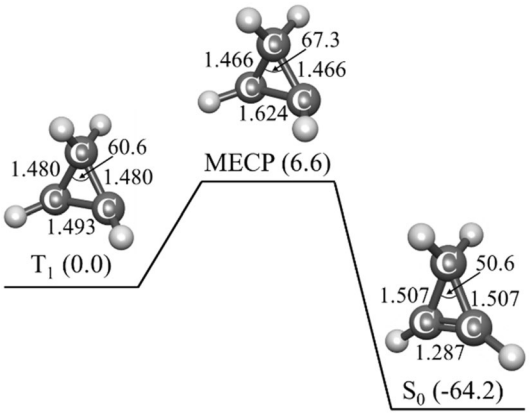

Fig. 8 The $T_1 \rightarrow S_0$ relaxation path in cyclopropene. The relative energies of the T_1 minimum, the S_0 minimum and MECP (kcal mol^{-1}) are in parentheses. The bond lengths and angles calculated at the B3LYP/cc-pVTZ level of theory are in Å and degrees

explained by the 1.0 kcal mol^{-1} discrepancy in the TS barrier (using the same barrier height of 53.2 kcal mol^{-1} in both analytical expressions reduces this difference to 18%). The difference between the NAST rate constant (67.8 s^{-1}) and the analytical constant obtained with Eq. (30) (101.0 s^{-1}) could be due to a finite accuracy of the numerical integration in NAST. For the isomerization to propanal, similar differences in the reaction rate constants calculated with different methods are observed. All calculated rate constants are in reasonable agreement with the experimental values for both isomerization reactions.

4.2 Spin-Forbidden Isomerization of Ni(dpp)Cl_2

This example demonstrates the forward and reverse rate constants calculation in a single NAST run. In addition to the overall rate constants, it predicts the rate constants between individual M_S components of two spin states. Spin-forbidden kinetics

of interconversion between the singlet (planar) and triplet (tetrahedral) isomers of Ni(dpp)Cl_2 complex (dpp = 1,3-bis(diphenylphosphino)propane) has been studied in acetonitrile [96]. To reduce the computational cost, the phenyl groups were replaced by methyls (Fig. 6). The optimized geometries and Hessians for singlet, triplet, and MECP structures were obtained with the M11-L density functional, implicit solvation model, and def2-TZVP basis set, as implemented in GAMESS. The SOC value of 135 cm^{-1} was calculated with the second-order multiconfigurational quasi-degenerate perturbation theory (MCQDPT2) using the CASSCF(2e, 4o) wave function averaged over the lowest energy singlet and triplet electronic states. The forward ($S_1 \rightarrow T_0$) rate constant calculated using the WC transition probability at 296 K (4.96×10^6 s^{-1}) agrees almost within one order of magnitude with the experimental value of 4.5×10^5 s^{-1}. However, the reverse ($T_0 \rightarrow S_1$) rate constant predicted to be 3.50×10^2 s^{-1} is significantly smaller than the experimental value of 6.0×10^5 s^{-1}, which could indicate that the barrier for the reverse reaction is overestimated due to the low level of electronic structure calculations and the reduced model size.

Calculations of the transition probabilities and rate constants between individual M_S components of the singlet and triplet states were carried out using the spin–orbit matrix elements ($z = -69.0 - 63.8i$ cm^{-1} and $b = 21.3$ cm^{-1}, as defined in Eq. 20) obtained from the same MCQDPT2 calculations. The M_S-specific rate constants $k_{M_S,M_{S'}}$ for the transitions between the $M_S = 0$ component of singlet state and three $M_{S'} = \pm 1$ and $M_{S'} = 0$ components of the triplet state, calculated using the LZ transition probability, are plotted in Fig. 7. The stronger couplings between the $M_S = 0$ component of the singlet state and the $M_{S'} = \pm 1$ components of the triplet result

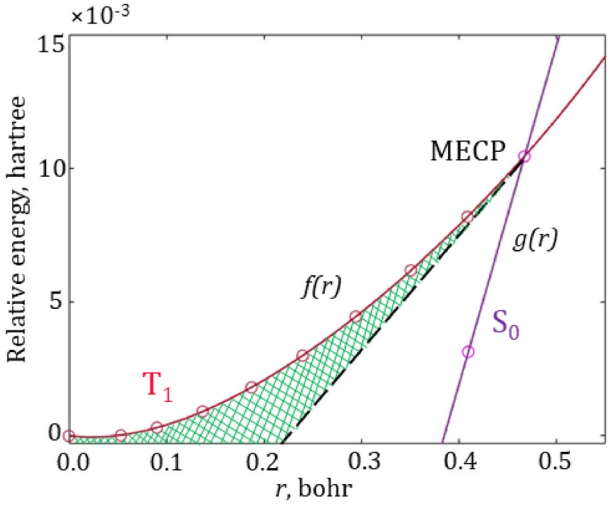

Fig. 9 Fitted $T_1 \rightarrow$ MECP $\rightarrow S_0$ reaction path. The circles mark the energies of the IRC geometries. The green area shows an increase in the tunneling barrier width compared to the linear model (dashed black line). For the rate constant calculations, the coefficients of the fitting polynomials ($f(r) = 0.092\ r^4 - 0.121\ r^3 + 0.093\ r^2 - 0.004\ r - 1.86 \times 10^{-6}$ and $g(r) = 0.127r - 0.048$) are included in the NAST input file

Table 2 The $T_1 \rightarrow S_0$ canonical rate constant (s^{-1}) at different temperatures

T, K	NAST	MESMER	Relative difference
100	1.52×10^{-16}	2.37×10^{-16}	−0.36
200	6.71×10^{-4}	7.88×10^{-4}	−0.15
300	1.19×10^{1}	1.29×10^{1}	−0.08
400	1.62×10^{3}	1.68×10^{3}	−0.03
500	3.16×10^{4}	3.09×10^{4}	0.02
600	2.33×10^{5}	2.13×10^{5}	0.09
700	9.81×10^{5}	8.43×10^{5}	0.16
800	2.91×10^{6}	2.35×10^{6}	0.24
900	6.85×10^{6}	5.18×10^{6}	0.32
1000	1.36×10^{7}	9.71×10^{6}	0.40
1100	2.41×10^{7}	1.62×10^{7}	0.49
1200	3.89×10^{7}	2.47×10^{7}	0.58
1300	5.85×10^{7}	3.52×10^{7}	0.66
1400	8.32×10^{7}	4.76×10^{7}	0.75
1500	1.13×10^{8}	6.17×10^{7}	0.83
1600	1.48×10^{8}	7.73×10^{7}	0.91
1700	1.88×10^{8}	9.42×10^{7}	1.00
1800	2.33×10^{8}	1.12×10^{8}	1.08
1900	2.82×10^{8}	1.31×10^{8}	1.15
2000	3.36×10^{8}	1.50×10^{8}	1.24

The relative difference between the NAST and MESMER values is defined as $(k_{NAST} - k_{MESMER})/k_{MESMER}$

in the faster population transfer, as evident from the $k_{0,\pm1}$ rate constant being larger than $k_{0,0}$.

4.3 $T_1 \rightarrow S_0$ Relaxation in Cyclopropene

This example demonstrates calculation of the rate constant using the ZN transition probability. Miller and Klippenstein published a detailed kinetics study of different reactions of C_3H_4, including those proceeding on multiple PESs with different spin multiplicities [97]. Here we consider the $T_1 \rightarrow S_0$ relaxation in cyclopropene (Fig. 8). The equilibrium geometries and Hessians of the S_0, T_1 states and MECP were obtained at the B3LYP/cc-pVTZ level of theory. The SOC constant of 4.0 cm^{-1} was calculated with the MCQDPT2 method based on the CASSCF(2,2) wave function averaged over the S_0 and T_1 states, using the same basis set. All calculations were performed in GAMESS. To calculate the $T_1 \rightarrow S_0$ rate constant with the ZN transition probability, the $T_1 \rightarrow$ MECP $\rightarrow S_0$ minimum energy reaction path was fitted with the *ircifit* tool using the geometries and energies generated by two IRC calculations starting from MECP and following to the T_1 and S_0 minima. The MECP $\rightarrow T_1$ path was fitted with the quartic polynomial, while the MECP $\rightarrow S_0$ path was approximated by a linear fit (Fig. 9).

The $T_1 \rightarrow S_0$ canonical rate constant calculated at 1000 K with the ZN transition probability (3.07×10^7 s^{-1}) is almost an order of magnitude smaller than the value obtained with the WC probability (1.24×10^8 s^{-1}). This difference can be explained by the fact that the linear-crossing WC model significantly underestimates the width of the tunneling barrier (Fig. 9). In contrast, the ZN model uses more realistic potential energy curves and predicts a wider barrier, leading to a significant reduction in the tunneling contribution to the rate constant. Table 2 compares the same rate constant calculated using the simple LZ transition probability with the values obtained by the MESMER 6.0 package [98]. There is reasonable agreement between the values predicted by the two packages. The larger discrepancies at high temperatures are attributed to the numerical integration errors in Eq. (2). It is important to note that these discrepancies in the rate constants are significantly smaller than the errors expected due to the limited accuracy of the MECP barrier calculated by commonly used electronic structure methods.

5 Conclusions

We introduced the NAST software package for predicting kinetics of spin-dependent processes, including intersystem crossings, spin-forbidden reactions, and spin crossovers. The package calculates both the microcanonical and canonical rate constants and can account for quantum tunneling, zero-point vibrational energy, and reaction path interference. Traditional single-state adiabatic TST calculations are also possible. The main strengths of NAST stem from its ability to (1) model nonadiabatic kinetics in large systems, (2) use high-level electronic structure methods for predicting molecular properties, which is critical for accurate kinetics calculations, and (3) study slow spin-dependent processes that present a great challenge for nonadiabatic molecular dynamics. Additional computational tools included in the NAST package simplify setting up kinetics calculations using molecular properties obtained with different electronic structure programs. The three presented examples demonstrate various capabilities of the NAST package. Future development will focus on multidimensional tunneling effects, accounting for MECP barrier recrossing, modeling spin-dependent processes in solution, and using an external magnetic field to control the kinetics of spin-dependent processes.

Supplementary Information The online version contains supplementary material available at https://doi.org/10.1007/s41061-022-00366-w.

Acknowledgements This work was supported by the National Science Foundation through a CAREER Award (CHE-1654547). We acknowledge Dr. Ryan Zaari for his contributions to the earlier version of the NAST package and thank Drs. Danil Kaliakin and Saikat Mukherjee for fruitful discussions.

Author contributions S.A.V. supervised the NAST package development. V.D.D., M.R., I.D.D., A.O.L. and R.C.M. wrote different parts of the code. V.D.D, M.R. and I.D.D. performed the electronic structure and kinetics calculations. All authors contributed to the preparation of the manuscript.

Funding This work was supported by the National Science Foundation through a CAREER Award (CHE 1654547).

Availability of data and material The input files for the electronic structure, NAST and MESMER calculations discussed in the main text are available in the SI.

Code availability The source code of the NAST package is available free of charge at https://github.com/svarganov/NAST.

Declarations

Conflict of interest The authors declare no conflict of interest.

References

1. Schröder D, Shaik S, Schwarz H (2000) Two-state reactivity as a new concept in organometallic chemistry. Acc Chem Res 33:139–145. https://doi.org/10.1021/ar990028j
2. Liao P, Carter EA (2013) New concepts and modeling strategies to design and evaluate photo-electro-catalysts based on transition metal oxides. Chem Soc Rev 42:2401–2422. https://doi.org/10.1039/c2cs35267b
3. Sun Y, Tang H, Chen K et al (2016) Two-state reactivity in low-valent iron-mediated C-H activation and the implications for other first-row transition metals. J Am Chem Soc 138:3715–3730. https://doi.org/10.1021/jacs.5b12150
4. Lykhin AO, Kaliakin DS, DePolo GE et al (2016) Nonadiabatic transition state theory: application to intersystem crossings in the active sites of metal-sulfur proteins. Int J Quantum Chem 116:750–761. https://doi.org/10.1002/qua.25124
5. Goodrow A, Bell AT, Head-Gordon M (2009) Are spin-forbidden crossings a bottleneck in methanol oxidation? J Phys Chem C 113:19361–19364. https://doi.org/10.1021/jp906603r
6. Kaliakin DS, Zaari RR, Varganov SA (2015) Effect of H_2 binding on the nonadiabatic transition probability between singlet and triplet states of the [NiFe]-hydrogenase active site. J Phys Chem A 119:1066–1073. https://doi.org/10.1021/jp510522z
7. Pohlman AJ, Kaliakin DS, Varganov SA, Casey SM (2020) Spin controlled surface chemistry: alkyl desorption from Si(100)-2×1 by nonadiabatic hydrogen elimination. Phys Chem Chem Phys 22:16641–16647. https://doi.org/10.1039/d0cp01913e
8. Zhao J, Wu W, Sun J, Guo S (2013) Triplet photosensitizers: from molecular design to applications. Chem Soc Rev 42:5323–5351. https://doi.org/10.1039/c3cs35531d
9. Zhao J, Chen K, Hou Y et al (2018) Recent progress in heavy atom-free organic compounds showing unexpected intersystem crossing (ISC) ability. Org Biomol Chem 16:3692–3701. https://doi.org/10.1039/c8ob00421h
10. Pordel S, Pickens RN, White JK (2021) Release of CO and production of $^1O_2$ from a Mn-BODIPY Photoactivated CO releasing molecule with visible light. Organometallics 40:2983–2994. https://doi.org/10.1021/acs.organomet.1c00331
11. Bogani L, Wernsdorfer W (2008) Molecular spintronics using single-molecule magnets. Nat Mater 7:179–186. https://doi.org/10.1038/nmat2133
12. Gaita-Ariño A, Luis F, Hill S, Coronado E (2019) Molecular spins for quantum computation. Nat Chem 11:301–309. https://doi.org/10.1038/s41557-019-0232-y
13. Goldman ML, Doherty MW, Sipahigil A et al (2015) State-selective intersystem crossing in nitrogen-vacancy centers. Phys Rev B 91:1–11. https://doi.org/10.1103/PhysRevB.91.165201
14. Bayliss SL, Laorenza DW, Mintun PJ et al (2020) Optically addressable molecular spins for quantum information processing. Science 370:1309–1312. https://doi.org/10.1126/science.abb9352
15. Ullah A, Cerdá J, Baldoví JJ et al (2019) In silico molecular engineering of dysprosocenium-based complexes to decouple spin energy levels from molecular vibrations. J Phys Chem Lett 10:7678–7683. https://doi.org/10.1021/acs.jpclett.9b02982

16. Mitschke U, Bäuerle P (2000) The electroluminescence of organic materials. J Mater Chem 10:1471–1507. https://doi.org/10.1039/a908713c
17. Goushi K, Yoshida K, Sato K, Adachi C (2012) Organic light-emitting diodes employing efficient reverse intersystem crossing for triplet-to-singlet state conversion. Nat Photonics 6:253–258. https://doi.org/10.1038/nphoton.2012.31
18. Endo A, Ogasawara M, Takahashi A et al (2009) Thermally activated delayed fluorescence from Sn^{4+}-porphyrin complexes and their application to organic light-emitting diodes—a novel mechanism for electroluminescence. Adv Mater 21:4802–4806. https://doi.org/10.1002/adma.200900983
19. Bergmann L, Hedley GJ, Baumann T et al (2016) Direct observation of intersystem crossing in a thermally activated delayed fluorescence copper complex in the solid state. Sci Adv 2:1–7. https://doi.org/10.1126/sciadv.1500889
20. Wada Y, Nakagawa H, Matsumoto S et al (2020) Organic light emitters exhibiting very fast reverse intersystem crossing. Nat Photonics 14:643–649. https://doi.org/10.1038/s41566-020-0667-0
21. Franzen S, Kiger L, Poyart C, Martin JL (2001) Heme photolysis occurs by ultrafast excited state metal-to-ring charge transfer. Biophys J 80:2372–2385. https://doi.org/10.1016/S0006-3495(01)76207-8
22. Wang W, Ye X, Demidov AA et al (2000) Femtosecond multicolor pump-probe spectroscopy of ferrous cytochrome C. J Phys Chem B 104:10789–10801. https://doi.org/10.1021/jp0008602
23. Dunietz BD, Dreuw A, Head-Gordon M (2003) Initial steps of the photodissociation of the CO ligated heme group. J Phys Chem B 107:5623–5629. https://doi.org/10.1021/jp0226376
24. Mara MW, Hadt RG, Reinhard ME et al (2017) Metalloprotein entatic control of ligand-metal bonds quantified by ultrafast x-ray spectroscopy. Science 356:1276–1280. https://doi.org/10.1126/science.aam6203
25. Falahati K, Tamura H, Burghardt I, Huix-Rotllant M (2018) Ultrafast carbon monoxide photolysis and heme spin-crossover in myoglobin via nonadiabatic quantum dynamics. Nat Commun 9:1–8. https://doi.org/10.1038/s41467-018-06615-1
26. Harvey JN, Aschi M (2003) Modelling spin-forbidden reactions: recombination of carbon monoxide with iron tetracarbonyl. Faraday Discuss 124:129–143. https://doi.org/10.1039/b211871h
27. Yang B, Gagliardi L, Truhlar DG (2018) Transition states of spin-forbidden reactions. Phys Chem Chem Phys 20:4129–4136. https://doi.org/10.1039/c7cp07227a
28. Jensen KP, Ryde U (2004) How O_2 binds to heme. Reasons for rapid binding and spin inversion. J Biol Chem 279:14561–14569. https://doi.org/10.1074/jbc.M314007200
29. Strickland N, Harvey JN (2007) Spin-forbidden ligand binding to the ferrous-heme group: Ab initio and DFT studies. J Phys Chem B 111:841–852. https://doi.org/10.1021/jp064091j
30. Harvey JN (2004) Spin-forbidden CO ligand recombination in myoglobin. Faraday Discuss 127:165–177. https://doi.org/10.1039/b314768a
31. Kahn O, Martinez CJ (1998) Spin-transition polymers: from molecular materials toward memory devices. Science 279:44–48. https://doi.org/10.1126/science.279.5347.44
32. Halder GJ, Kepert CJ, Moubaraki B et al (2002) Guest-dependent spin crossover in a nanoporous molecular framework material. Science 298:1762–1765. https://doi.org/10.1126/science.1075948
33. Gütlich PGH (2004) Spin crossover in transition metal compounds I-III. Top Curr Chem 23(234):235
34. Halcrom MA (2013) Spin-crossover materials, properities and applications. Wiley, Hoboken
35. Senthil Kumar K, Ruben M (2017) Emerging trends in spin crossover (SCO) based functional materials and devices. Coord Chem Rev 346:176–205. https://doi.org/10.1016/j.ccr.2017.03.024
36. Real JA, Gaspar AB, Carmen Muñoz M (2005) Thermal, pressure and light switchable spin-crossover materials. Dalt Trans 12:2062–2079. https://doi.org/10.1039/b501491c
37. Bonhommeau S, Molnár G, Galet A et al (2005) One shot laser pulse induced reversible spin transition in the spin-crossover complex $[Fe(C_4H_4N_2)\{Pt(CN)_4\}]$ at room temperature. Angew Chemie Int Ed 44:4069–4073. https://doi.org/10.1002/anie.200500717
38. Gaspar AB, Ksenofontov V, Seredyuk M, Gütlich P (2005) Multifunctionality in spin crossover materials. Coord Chem Rev 249:2661–2676. https://doi.org/10.1016/j.ccr.2005.04.028
39. Muller RN, Vander EL, Laurent S (2003) Spin transition molecular materials: Intelligent contrast agents for magnetic resonance imaging. J Am Chem Soc 125:8405–8407. https://doi.org/10.1021/ja0349599
40. Beck M (2000) The multiconfiguration time-dependent Hartree (MCTDH) method: a highly efficient algorithm for propagating wavepackets. Phys Rep 324:1–105. https://doi.org/10.1016/S0370-1573(99)00047-2

41. Barbatti M (2011) Nonadiabatic dynamics with trajectory surface hopping method. Wiley Interdiscip Rev Comput Mol Sci 1:620–633. https://doi.org/10.1002/wcms.64
42. Curchod BFE, Martinez TJ (2018) Ab initio nonadiabatic quantum molecular dynamics. Chem Rev 118:3305–3336. https://doi.org/10.1021/acs.chemrev.7b00423
43. Mai S, Marquetand P, González L (2018) Nonadiabatic dynamics: the SHARC approach. Wiley Interdiscip Rev Comput Mol Sci 8:1–23. https://doi.org/10.1002/wcms.1370
44. Hammes-Schiffer S, Tully JC (1995) Nonadiabatic transition state theory and multiple potential energy surface molecular dynamics of infrequent events. J Chem Phys 103:8513–8527. https://doi.org/10.1063/1.470162
45. Shenvi N, Subotnik JE, Yang W (2011) Simultaneous-trajectory surface hopping: a parameter-free algorithm for implementing decoherence in nonadiabatic dynamics. J Chem Phys 134:144102. https://doi.org/10.1063/1.3575588
46. Curchod BFE, Rauer C, Marquetand P et al (2016) Communication: GAIMS—generalized ab initio multiple spawning for both internal conversion and intersystem crossing processes. J Chem Phys 144:101102. https://doi.org/10.1063/1.4943571
47. Fedorov DA, Pruitt SR, Keipert K et al (2016) Ab initio multiple spawning method for intersystem crossing dynamics: spin-forbidden transitions between $^3B_1$ and $^1A_1$ states of GeH_2. J Phys Chem A 120:2911–2919. https://doi.org/10.1021/acs.jpca.6b01406
48. Fedorov DA, Lykhin AO, Varganov SA (2018) Predicting intersystem crossing rates with AIMS-DFT molecular dynamics. J Phys Chem A 122:3480–3488
49. Mukherjee S, Fedorov DA, Varganov SA (2021) Modeling spin-crossover dynamics. Annu Rev Phys Chem 72:515–540. https://doi.org/10.1146/annurev-physchem-101419-012625
50. Harvey JN (2007) Understanding the kinetics of spin-forbidden chemical reactions. Phys Chem Chem Phys 9:331–343. https://doi.org/10.1039/b614390c
51. Harvey JN, Aschi M (1999) Spin-forbidden dehydrogenation of methoxy cation: a statistical view. Phys Chem Chem Phys 1:5555–5563. https://doi.org/10.1039/a907723e
52. Harvey JN (2014) Spin-forbidden reactions: Computational insight into mechanisms and kinetics. Wiley Interdiscip Rev Comput Mol Sci 4:1–14. https://doi.org/10.1002/wcms.1154
53. Cui Q, Morokuma K, Bowman JM, Klippenstein SJ (1999) The spin-forbidden reaction $CH(^2\Pi)+N_2 \rightarrow HCN+N(^4S)$ revisited. II. Nonadiabatic transition state theory and application. J Chem Phys 110:9469–9482. https://doi.org/10.1063/1.478949
54. Lorquet JC, Leyh-Nihant B (1988) Nonadiabatic unimolecular reactions. 1. A statistical formulation for the rate constants. J Phys Chem 92:4778–4783. https://doi.org/10.1021/j100327a043
55. Nikitin EE, Umanskii SY (1984) Theory of slow atomic collisions. Springer, Berlin
56. Zhao Y, Mil'nikov G, Nakamura H (2004) Evaluation of canonical and microcanonical nonadiabatic reaction rate constants by using the Zhu-Nakamura formulas. J Chem Phys 121:8854–8860. https://doi.org/10.1063/1.1801971
57. Marks AJ (2001) Nonadiabatic transition-state theory: a Monte Carlo study of competing bond fission processes in bromoacetyl chloride. J Chem Phys 114:1700–1708. https://doi.org/10.1063/1.1333702
58. McLafferty FJ, George TF (1976) On nonadiabatic transition state theory. Chem Phys Lett 37:67–71. https://doi.org/10.1016/0009-2614(76)80163-7
59. Lykhin AO, Varganov SA (2020) Intersystem crossing in tunneling regime: $T_1 \rightarrow S_0$ relaxation in thiophosgene. Phys Chem Chem Phys 22:5500–5508. https://doi.org/10.1039/c9cp06956a
60. Truhlar DG, Garrett BC, Klippenstein SJ (1996) Current status of transition-state theory. J Phys Chem 100:12771–12800. https://doi.org/10.1021/jp953748q
61. Truhlar DG, Garrett BC (1984) Variational transition state theory. Ann Rev Phys Chem 35:159–189. https://doi.org/10.1146/annurev.pc.35.100184.001111
62. Laidler KJ, King MC (1983) The development of transition-state theory. J Phys Chem 87:2657–2664. https://doi.org/10.1021/j100238a002
63. Garrett BC, Truhlar DG (1979) Generalized transition state theory. Classical mechanical theory and applications to collinear reactions of hydrogen molecules. J Phys Chem 83:1052–1079. https://doi.org/10.1021/j100471a031
64. Miller WH (1998) "Direct" and "correct" calculation of canonical and microcanonical rate constants for chemical reactions. J Phys Chem A 102:793–806. https://doi.org/10.1021/jp973208o
65. Bao JL, Truhlar DG (2017) Variational transition state theory: Theoretical framework and recent developments. Chem Soc Rev 46:7548–7596. https://doi.org/10.1039/c7cs00602k

66. Marian CM (2012) Spin-orbit coupling and intersystem crossing in molecules. Wiley Interdiscip Rev Comput Mol Sci 2:187–203. https://doi.org/10.1002/wcms.83
67. Fedorov DG, Koseki S, Schmidt MW, Gordon MS (2003) Spin-orbit coupling in molecules: chemistry beyond the adiabatic approximation. Int Rev Phys Chem 22:551–592. https://doi.org/10.1080/0144235032000101743
68. Marian CM (2001) Spin-orbit coupling in molecules. In: Lipkowitz KB, Boyd DB (eds) Reviews in computational chemistry. Wiley, Hoboken, pp 99–204
69. Marian CM (2021) Understanding and controlling intersystem crossing in molecules. Annu Rev Phys Chem 72:617–640. https://doi.org/10.1146/annurev-physchem-061020-053433
70. Zhu C, Nakamura H (1994) Theory of nonadiabatic transition for general two-state curve crossing problems. I. Nonadiabatic tunneling case. J Chem Phys 101:10630–10647. https://doi.org/10.1063/1.467877
71. Fernández-Ramos A, Ellingson BA, Meana-Pañeda R et al (2007) Symmetry numbers and chemical reaction rates. Theor Chem Acc 118:813–826. https://doi.org/10.1007/s00214-007-0328-0
72. Lykhin AO (2019) Predicting kinetics of spin-forbidden unimolecular reactions with nonadiabatic transition state theory. Ph.D. Dissertation, University of Nevada, Reno
73. Delos JB (1973) On the reactions of N_2 with O. J Chem Phys 59:2365–2369. https://doi.org/10.1063/1.1680345
74. Dashevskaya EI, Nikitin EE (2017) Uniform airy approximation for nonadiabatic transitions in a curve-crossing weak-coupling. Z Phys Chem 232:311–323. https://doi.org/10.1515/zpch-2017-1025
75. Nakamura H (2012) Nonadiabatic transition: concepts, basic theories and applications, 2nd edn. World Scientific, Berlin
76. Zhu C, Teranishi Y, Nakamura H (2001) Nonadiabatic transitions due to curve crossings: complete solutions of the landau-zener-stueckelberg problems and their applications. In: Prigogine I, Rice SA (eds) Advances in chemical physics. Wiley Online Librabry, pp 127–133
77. Zhu C, Nakamura H, Re N, Aquilanti V (1992) The two-state linear curve crossing problems revisited. I. Analysis of Stokes phenomenon and expressions for scattering matrices. J Chem Phys 97:1892–1904. https://doi.org/10.1063/1.463178
78. Zhu C, Nakamura H (1992) The two-state linear curve crossing problems revisited. II. Analytical approximations for the Stokes constant and scattering matrix: the Landau-Zener case. J Chem Phys 97:8497–8514. https://doi.org/10.1063/1.464814
79. Zhu C, Nakamura H (1994) Two-state linear curve crossing problems revisited. IV. The best analytical formulas for scattering matrices. J Chem Phys 101:4855–4866. https://doi.org/10.1063/1.468505
80. Melissas VS, Truhlar DG, Garrett BC (1992) Optimized calculations of reaction paths and reaction-path functions for chemical reactions. J Chem Phys 96:5758–5772. https://doi.org/10.1063/1.462674
81. Kuki A (1993) Adiabaticity factor for electron transfer in the multimode case: an energy velocity perspective. J Phys Chem 97:13107–13116. https://doi.org/10.1021/j100152a013
82. Bracewell RN (2000) The fourier transform and its applications, 3d edn. McGraw-Hill, New York
83. Baer T, Hase WL (1996) Unimolecular reaction dynamics: theory and experiments. Oxford University Press, Oxford
84. Green NJB (2003) Unimolecular kinetics part 1. The reaction step. Elsevier, Hoboken
85. Lykhin AO, Truhlar DG, Gagliardi L (2021) Role of triplet states in the photodynamics of aniline. J Am Chem Soc 143:5878–5889. https://doi.org/10.1021/jacs.1c00989
86. Galano A, Alvarez-Idaboy JR (2013) A computational methodology for accurate predictions of rate constants in solution: application to the assessment of primary antioxidant activity. J Comput Chem 34:2430–2445. https://doi.org/10.1002/jcc.23409
87. Dzib E, Cabellos JL, Ortíz-Chi F et al (2019) Eyringpy: a program for computing rate constants in the gas phase and in solution. Int J Quant Chem 119:11–13. https://doi.org/10.1002/qua.25686
88. Garrett BC, Schenter GK (1994) Variational transition state theory for activated chemical reactions in solution. Int Rev Phys Chem 13:263–289. https://doi.org/10.1080/01442359409353296
89. Truhlar D, Pliego JR (2008) Transition state theory and chemical reaction dynamics in solution. In: Mennucci B, Cammi R (eds) Continuum solvation models in chemical physics: theory and application. Wiley, Hoboken
90. Hall DG (1986) The status of transition-state theory in non-ideal solutions and application of Kirkwood-Buff theory to the transition state. J Chem Soc Faraday Trans 2: Mol Chem Phys 82:1297–1303. https://doi.org/10.1039/F29868201297

91. Henriksen NE, Hansen FY (2018) Static solvent effects, transition-state theory. Theories of molecular reaction dynamics: the microscopic foundation of chemical kinetics. Oxford University Press, Oxford
92. Barca GMJ, Bertoni C, Carrington L et al (2020) Recent developments in the general atomic and molecular electronic structure system. J Chem Phys 152:154102. https://doi.org/10.1063/5.0005188
93. Werner HJ, Knowles PJ, Manby FR et al (2020) The Molpro quantum chemistry package. J Chem Phys 152:144107. https://doi.org/10.1063/5.0005081
94. Dubnikova F, Lifshitz A (2000) Isomerization of propylene oxide. Quantum chemical calculations and kinetic modeling. J Phys Chem A 104:4489–4496. https://doi.org/10.1021/jp004038+
95. Lifshitz A, Tamburu C (1994) Isomerization and decomposition of propylene oxide. Studies with a single-pulse shock tube. J Phys Chem 98:1161–1170. https://doi.org/10.1021/j100055a020
96. McGarvey JJ, Wilson J (1975) Photochemical perturbation and chemical relaxation of the planar—tetrahedral equilibrium in a di(tertiary phosphine) complex of nickel(II). J Am Chem Soc 97:2531–2532. https://doi.org/10.1021/ja00842a034
97. Miller JA, Klippenstein SJ (2003) From the multiple-well master equation to phenomenological rate coefficients: reactions on a C_3H_4 potential energy surface. J Phys Chem A 107:2680–2692. https://doi.org/10.1021/jp0221082
98. Glowacki DR, Liang CH, Morley C et al (2012) MESMER: an open-source master equation solver for multi-energy well reactions. J Phys Chem A 116:9545–9560. https://doi.org/10.1021/jp3051033

Authors and Affiliations

Vsevolod D. Dergachev[1] · Mitra Rooein[1] · Ilya D. Dergachev[1] · Aleksandr O. Lykhin[1,2] · Robert C. Mauban[1] · Sergey A. Varganov[1]

[1] Department of Chemistry, University of Nevada, Reno, 1664 N. Virginia Street, Reno, NV 89557-0216, USA

[2] Present Address: Department of Chemistry, The University of Chicago, Chicago, IL 60637, USA

Preflight Results

Document Information

Title:	NAST: Nonadiabatic Statistical Theory Package for Predicting Kinetics of Spin-Dependent Processes
Author:	Vsevolod D. Dergachev
Creator:	Springer
Producer:	Acrobat Distiller 10.1.8 (Windows); modified using iText® 5.3.5 ©2000-2012 1T3XT BVBA (SPRINGER SBM; licensed

Preflight Information

Profile:	Convert to PDF/A-1b
Version:	Qoppa jPDFPreflight v2021R1.00
Date:	Apr 29, 2022 12:35:36 AM

Legend: (X) - Can NOT be fixed by PDF/A-1b conversion.
(!X) - Could be fixed by PDF/A-1b conversion. User chose to be warned in PDF/A settings.

Page 6 Results

(X) Font widths must be the same in both the font dictionary and the embedded font file.
(X) Font widths must be the same in both the font dictionary and the embedded font file.